Visualization of the local contribution to the nodal surface of a many-fermion wave function

A. C. Calder,[1] M. R. Curry,[2] R. M. Panoff,[3] and Y. J. Wong[4]
[1]*Department of Physics and Astronomy, Vanderbilt University, Nashville, Tennessee 37235*
[2]*North Carolina Supercomputing Center, Research Triangle Park, North Carolina 27709*
[3]*The Shodor Education Foundation, Inc., Durham, North Carolina 27701*
[4]*IBM Corporation, RISC/6000 System Division, Poughkeepsie, New York 12601-5400*
(Received 23 October 1995)

An essential part of variational Monte Carlo or Green's function Monte Carlo (GFMC) algorithms is the trial wave function. In the case of particles obeying Fermi statistics, this wave function is antisymmetric and cannot be interpreted directly as a probability distribution, thereby making calculations difficult. Some progress can be made in GFMC algorithms, however, by requiring the trial wave function to have the same ''fixed'' nodes as the variational function. The sensitivity of the energy to changes in the nodal surface has remained a significant unresolved issue for two reasons: (a) the many-dimensional nodal surface is hard to quantify or visualize and (b) it has been difficult to vary this surface in a controlled fashion. As a first step toward gaining further information, we have developed a method of quantifying the many-dimensional nodal surface by creating and visually characterizing a related surface. The related surface is the surface of the local volume in which any given particle can range without changing the overall sign of the wave function, and this surface is mapped for different configurations and wave functions. A comparison of these surfaces allows us to characterize the local contributions to the nodal surface of a particular wave function and thereby visually differentiate between different types of wave functions. We show that introducing backflow correlations into the trial wave function results in a constrained volume with the undesired effect of significantly slowing down GFMC calculations. This study demonstrates that advanced visualization methods can serve a useful role in the process of algorithm development rather than just in the presentation of results. [S1063-651X(96)00505-3]

PACS number(s): 02.70.Lq

I. INTRODUCTION

A major focus of theoretical physics in general and many-body theory in particular is the development of computational methods for accurate and efficient first-principles calculations of the *macroscopic* properties of quantum systems from the *microscopic* interactions between particles in the system. Liquid ^{3}He has long served as the testing ground for diverse many-body calculational schemes because many of its properties are more experimentally accessible than other fermion systems such as nuclear matter [1–8]. A simple state-independent interaction provides an accurate description of the Hamiltonian of bulk ^{3}He, yet this interaction is strong enough to produce large correlations between the atoms.

Serving initially only as a ''benchmark'' for other more approximate calculations, the quantum Monte Carlo method has proven itself as one of the most powerful tools of the trade. The development and refinement of both variational and Green's function Monte Carlo methods and their application to helium systems stand as major achievements in computational science, while demonstrating the ability of large-scale computation to alter the direction of theoretical physics.

The application of quantum Monte Carlo methods to extended boson systems such as liquid ^{4}He, though requiring significant care and sophistication, has been straightforward compared to the arduous efforts aimed at applying these methods to fermion systems such as liquid ^{3}He. Since only a positive probability distribution can be represented as a list of particle coordinates—the key results of a quantum Monte Carlo (QMC) calculation are sets of configurations of particle coordinates drawn from a specified distribution—difficulties arise due to the antisymmetric nature of the fermion wave function. These difficulties are well known in the many areas of physics that have applied the quantum Monte Carlo method, from atomic and condensed matter physics back to the nuclear matter problem that gave rise to the many-body discipline [8,9]. The variational Monte Carlo method avoids the problem by dealing with distributions of particle coordinates drawn from a distribution proportional to the *square* of the wave function. In Green's function Monte Carlo (GFMC) calculations, however, the wave function itself must be sampled and the statistical error increases exponentially as the calculation proceeds.

An important, widely used variation of the GFMC method is the fixed-node approximation [10,11] in which the wave function is sampled in a domain of constant sign, within the nodal surface of an appropriate trial wave function. While the fixed-node approximation yields a rigorous upper bound with arbitrarily small statistical error, there is no *a priori* way of estimating how far from the ground-state energy eigenvalue the fixed-node energy may be. Furthermore, for wave functions with different nodal surfaces, the energies are very similar and sometimes statistically indistinguishable. Consequently, one is left asking whether or not the energy is sensitive to the details of the nodal surface. To date, there has been no clear way to estimate how much the nodal surface changes from one wave function parametrization to another. Therefore, prior to the present work, one could only guess whether the small energy shifts are due to small changes in the nodal surface of the wave function—in which case we would say that the energy is rather sensitive to the nodes—or

due to large changes in the nodes, leading to a conclusion that the energy is in fact rather insensitive to the nodes of the trial wave function.

What limits an even greater use of the quantum Monte Carlo method in physics and chemistry is sometimes its nearly prohibitive computational load. Consequently, in order to make these methods more accessible to the scientific community, our research focus has shifted from the application of exact but inefficient implementations of the QMC method in a variety of strongly correlated systems to a much-needed further refinement and parallel implementation of algorithms that can take advantage of advances in high performance computing technologies. Until recently, there has been very little application of scientific visualization in quantum Monte Carlo studies of ^{3}He since there are only a limited number of ways to display the principle *result* of our computation, that the experimental value for the energy per atom in the liquid is essentially reproduced by theory, $E=-2.4$ K. Surprising even ourselves, however, we have learned that visualization methods an be effectively applied to uncover previously unimagined paths toward more efficient algorithms by allowing us to ''see'' the bottlenecks in the *process* of the computation. This paper presents the results of our computational and visualization efforts in a study of the ground-state properties of liquid ^{3}He.

II. BASICS OF THE QUANTUM MONTE CARLO METHOD

The quantum Monte Carlo method encompasses several numerical methods that seek to directly solve the Schrödinger equation

$$H\Psi_0=E\Psi_0 \tag{1}$$

to obtain the ground-state wave function Ψ_0 for a given Hamiltonian H with energy eigenvalue E, without recourse to uncontrolled approximations. A nonrelativistic system of N helium atoms which interact via static two-body forces only has a Hamiltonian of the form

$$H=\frac{\hbar^2}{2m}\sum_{i=1}^{N}-\nabla_i^2+\sum_{1\leqslant i<j\leqslant N}v(r_{ij}). \tag{2}$$

The pair interaction $v(r_{ij})$ for the helium systems is taken to be the HFDHE2 interaction of Aziz *et al.* [12], which yields excellent agreement with experiment [1,13].

For two reasons, accurate variational calculations yielding a good ground-state trial function are an essential preliminary to practical and reliable GFMC calculations. In the first place, improved trial wave functions significantly reduce the statistical error by initiating the iterative calculation closer to the ground state. Moreover, an improved importance function acts to suppress population fluctuations. A physically motivated trial wave function of modified Feenberg form [14] is

$$\Psi_T=\psi_3 D, \tag{3}$$

where

$$\psi_3=\exp\left[-\frac{1}{2}\sum_{i<j}\tilde{u}(r_{ij})-\frac{\lambda_T}{4}\sum_l\sum_{i<j\neq l}\xi(r_{li})\xi(r_{lj})\vec{r}_{li}\cdot\vec{r}_{lj}\right], \tag{4}$$

$$\tilde{u}(r)=u(r)-\lambda_T\xi^2(r)r^2, \tag{5}$$

and D is the determinant that builds the required antisymmetry of the wave function. This ansatz includes explicit two- and three-body correlations [4]. The two-body correlation $u(r_{ij})$ is an appropriately scaled solution of an Euler-Lagrange equation obtained from Fermi hypernetted chain methods [15] or the solution of a parametrized two-body Schrödinger-like equation [16]. The triplet correlations are parametrized as

$$\xi(r)=\exp\left[-\left(\frac{r-r_T}{w_T}\right)^2\right]. \tag{6}$$

Different choices for the determinant D in Eq. (3) would be expected to result in different nodal surfaces. A simple choice for D is a Slater determinant of plane wave orbitals, which would be most appropriate for a noninteracting Fermi gas

$$D=\det(\exp[i\vec{k}_i\cdot\vec{r}_j]). \tag{7}$$

An alternative choice builds in momentum-dependent correlations to incorporate ''backflow'' effects [5]

$$D=\det\left\{\exp\left[i\vec{k}_i\cdot\left(\vec{r}_j+\sum_{l\neq j}\eta(r_{ij})\vec{r}_{lj}\right)\right]\right\}, \tag{8}$$

where

$$\eta(r)=\lambda_B\exp\left[-\left(\frac{r-r_B}{w_B}\right)^2\right]+\frac{\lambda_B'}{r^3}. \tag{9}$$

For the purposes of this paper, since we use the same two- and three-body correlations, we will distinguish the choice of wave function by simply referring to either a Slater wave function [Eqs. (3) and (7)] or a backflow wave function [Eqs. (3) and (8)]. In either case, the wave function is required to be periodic, so that all correlations are smoothed to zero at a distance equal to half the side of the simulation volume $r_{\max}$. Since the correlations that minimize the variational energy for liquid ^{3}He are relatively short ranged, this finite-size adaptation has no real effect on the magnitude of the correlations. Longer-range correlations may be studied with larger numbers of particles in increasingly larger periodic boxes. The calculations that we have done to date, however, have concentrated on 54 particles. Finite-size effects, though not negligible, are small enough that the fundamental physics may be displayed by these quantum simulations [17].

In variational calculations, the expectation value of the Hamiltonian, an upper bound to the ground-state energy E_0, may be evaluated as

$$E_0 \leqslant E_v = \frac{\int \Psi_T^*(R) H \Psi_T(R) dR}{\int \Psi_T^*(R) \Psi_T(R) dR}$$

$$= \int \frac{H\Psi_T(R)}{\Psi_T(R)} \frac{\Psi_T^*(R)\Psi_T(R) dR}{\int \Psi_T^*(R)\Psi_T(R) dR}. \quad (10)$$

The second form of the integral is easily calculated using the method of Metropolis *et al.* [18], usually with a low variance answer since $H\Psi_T(R)/\Psi_T(R)$ is nearly constant if $\Psi_T(R)$ is close to the true ground-state wave function. A good trial wave function minimizes Eq. (10) and its variance.

The optimum set of variational parameters [1] obtained for a system of 54 particles at the experimental equilibrium density for the backflow trial function above are $\lambda_T = -180$, $r_T = 0.66\sigma$, $w_T = 0.50\sigma$, $\lambda_B = 0.14$, $r_B = 0.74\sigma$, $w_B = 0.54\sigma$, and $\lambda_B' = 0.15\sigma^3$, where $\sigma = 2.556$ Å. In the Monte Carlo calculations, no approximations are necessary in evaluating the variational upper bound, subject to the caveat that the calculation refers to a finite number of particles with periodic boundary conditions. As the calculation proceeds, lists of particle coordinates, known as configurations, are written on disk. These configurations may be analyzed to compute other properties besides the energy. They also serve as input to Green's function Monte Carlo calculations, which iterate these configurations towards the true ground state.

The GFMC method [19,20] is based upon the fact that the Schrödinger equation is equivalent to a diffusion equation in imaginary time. The GFMC algorithm is implemented by choosing a set of points $\{R\}$ in configuration space and iterating the equation

$$\Psi^{n+1}(R) = E_T \int G(R,R')\Psi^n(R') dR'. \quad (11)$$

Although the Green's function is not known analytically, it can be sampled exactly through the use of an ancillary random walk. The GFMC method has been applied to macroscopic bosonic systems, such as liquid ^{4}He, with great success. It has also been applied to few-body fermion systems where elaborate sampling schemes are possible because the dimensionality of the system is small [9].

Exact GFMC treatment of many-body fermion systems, however, has proven to be very elusive. The requirement that the wave function be antisymmetric is a global property that is difficult to incorporate successfully into the diffusion algorithm, which is local in character. The fact that the wave function is not positive definite introduces a statistical error that grows exponentially as Eq. (11) is iterated. Fermion algorithms typically introduce two positive populations, the difference of which corresponds to the desired antisymmetric wave function

$$\Psi^A = \Psi^+ - \Psi^-. \quad (12)$$

A wide set of fermion GFMC algorithms can be viewed in the framework of mirror potentials as shown by Carlson and Kalos [21] and applied to ^{3}He by Panoff and Carlson [1]. By introducing two coupled equations

$$[H(R) + c(R)\Psi^+(R)]\Psi^-(R) = E\Psi^-(R), \quad (13)$$

$$[H(R) + c(R)\Psi^-(R)]\Psi^+(R) = E\Psi^+(R) \quad (14)$$

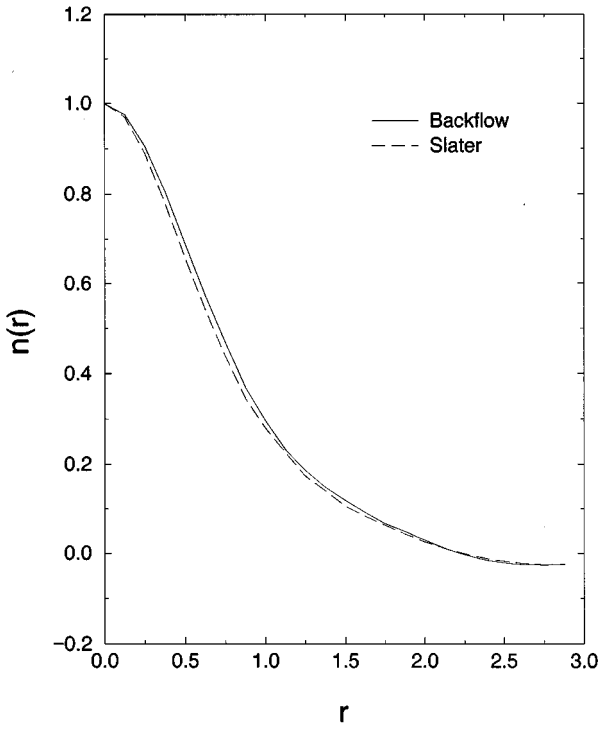

FIG. 1. One-body density matrix $n(r)$ in ^{3}He for two choices of variational wave function. Dashed line, Jastrow plus triplets plus Slater determinant; solid line, Jastrow plus triplets plus backflow. All distances are in units of $\sigma = 2.556$ Å.

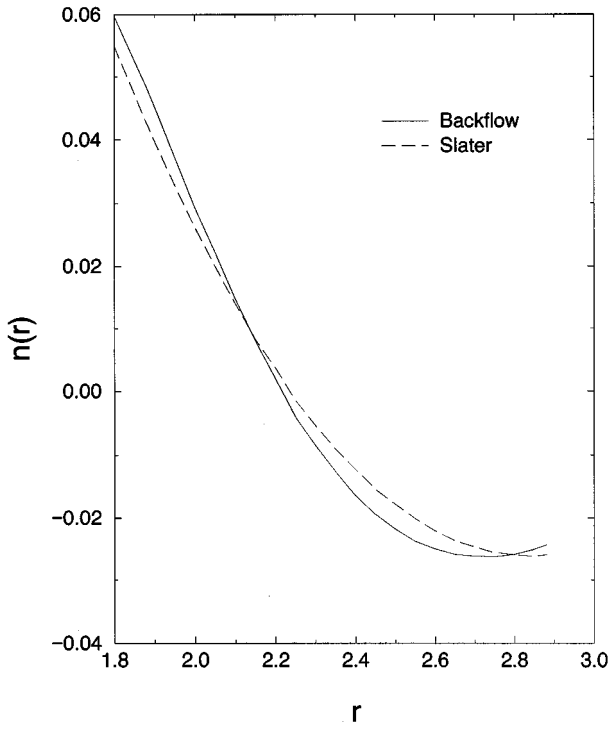

FIG. 2. One-body density matrix $n(r)$ in ^{3}He for two choices of variational wave function, larger-r detail. Dashed line, Jastrow plus triplets plus Slater determinant; solid line, Jastrow plus triplets plus backflow. All distances are in units of $\sigma = 2.556$ Å.

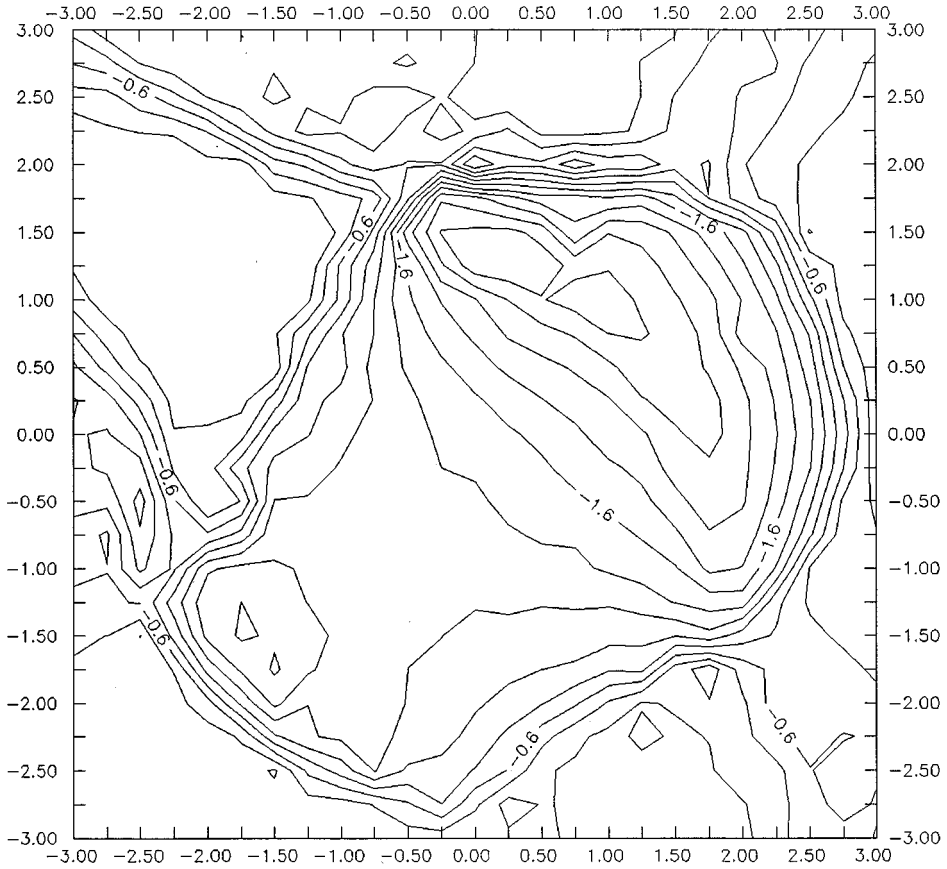

FIG. 3. Topological plot showing the lower half of the nodal volume generated from a Slater wave function.

and making an appropriate choice of the mirror potentials $c(R)\Psi^{\pm}(R)$, it is possible, in principle, to retain two stable and distinct positive populations for Ψ^{+} and Ψ^{-} such that the difference is a solution to the original Schrödinger equation.

The fixed-node approximation, whose development predates the mirror potential description, is a limiting case of Eqs. (13) and (14), corresponding to the limit $c(R)\rightarrow\infty$. The diffusion of the two populations is restricted thus to two isolated regions in configuration space. This prescription yields an upper bound to the true ground-state energy and leads to the lowest-energy wave function with the same nodes as the trial function. At each iteration, for each particle in a configuration, the Green's function is sampled in a domain of constant sign in Ψ. Enigmatically, when using backflow wave functions as the generating and importance function, we have been forced to make these domains much smaller to guarantee a constant sign. This results in a slower calculation requiring many more steps in imaginary time than when using a Slater wave function. Different-sized domains would seem to be strong evidence that the nodal surfaces of the two wave functions could be very different. In Table I, taken from Ref. [1], results for the energy per particle obtained at the experimental equilibrium density for several different trial wave functions of ^{3}He are collected. What is readily apparent is that the energy results are similar for different choices of wave function. Energies that are so similar would seem to suggest that the nodal surfaces could actually be quite similar, at least in some average sense. Particular choice for the functional forms of Jastrow, triplet, and backflow correlations, along with the values for the parameters in these functions, may be quite different while yielding very similar variational energies. However, other properties of the system at the variational level could still be very different [17]. Identifying some features that readily distinguish one choice of wave function from another has been a major goal of this work.

Both variational and GFMC calculations yield configura-

TABLE I. Results of Monte Carlo calculations for 54 ^{3}He atoms in a periodic box at $\rho\sigma^3=0.273$, where $\sigma=2.556$ Å. All energies are in K per particle. Results are from Ref. [1].

Method	E^*	β	Energy	$\langle T\rangle$	$\langle V\rangle$
Variational			-2.13 ± 0.02	12.22 ± 0.03	-14.35 ± 0.02
GFMC (mirror potential)	-2.30	60.0	-2.24 ± 0.04	12.33 ± 0.14	-14.57 ± 0.14
GFMC (mirror potential)	-2.35	70.0	-2.32 ± 0.07	12.22 ± 0.20	-14.54 ± 0.20
GFMC (mirror potential)	-2.40	70.0	-2.27 ± 0.03	12.42 ± 0.16	-14.69 ± 0.16
GFMC (mirror potential)	-2.35	80.0	-2.30 ± 0.04	12.34 ± 0.14	-14.64 ± 0.14
GFMC (fixed node)			-2.37 ± 0.01	12.28 ± 0.04	-14.65 ± 0.03

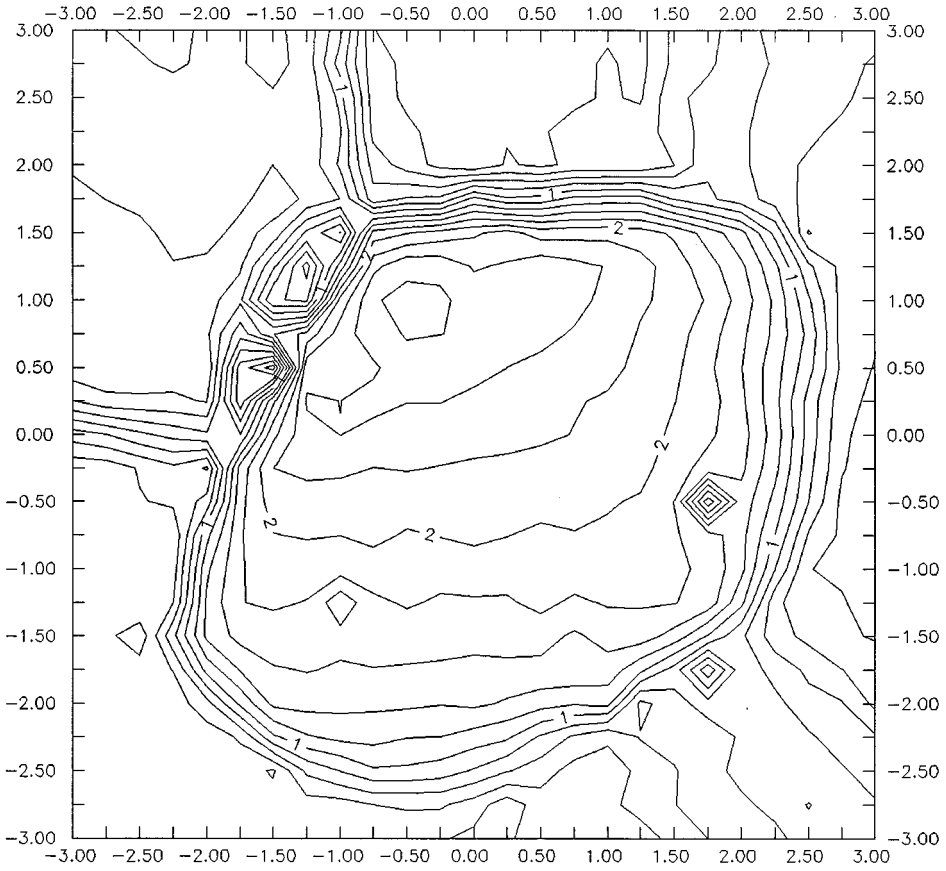

FIG. 4. Topological plot showing the upper half of the nodal volume generated from a Slater wave function.

tions, that is, lists of particle coordinates drawn from a probability density that is proportional to Ψ^2 for the VMC algorithm and to Ψ itself for the GFMC algorithm. These configurations may be analyzed to determine other properties of the systems. For instance, Table I also gives the kinetic energy $\langle T\rangle$ and potential energy $\langle V\rangle$ at equilibrium density. For every case, the kinetic energy per particle is between 12 and 12.5 K. For a variety of wave functions, there is actually very little percent change in the kinetic or potential energies calculated separately. As the wave function is improved, with an assumed greater degree of overlap with the ground state as higher-order correlations are included, there remains the sensitive cancellation of quantities of roughly the same magnitude.

These same configurations may be further analyzed [3,17,21] to give the one-body density matrix $n(\vec{r})$ and the momentum distribution $n(\vec{k})$ at k vectors contained within the simulation box. The one-body density matrix is the Fourier transform of the momentum distribution

$$n(\vec{r}) = \int e^{i\vec{k}\cdot\vec{r}} n(\vec{k})\, d\vec{k} = \left\langle \frac{\Psi(r_1, r_2, \ldots, r_i+\vec{r}, \ldots, r_n)}{\Psi(r_1, r_2, \ldots, r_i, \ldots, r_n)} \right\rangle \qquad (15)$$

and is a measure of the change in the wave function for a given displacement r. The expectation value in Eq. (15) is evaluated simply by moving particle i by an amount r and averaging the ratio of the wave functions over an ensemble of configurations. Two different methods may be used in this analysis. The first method computes $n(r)$ by moving particle i in the configurations a random amount giving the best values for $n(k)$ at specific k vectors. Alternatively, one determines $n(r)$ by moving particle i in increments of dr along a prescribed direction, yielding precise values of $n(r)$ at small r.

III. VISUAL CHARACTERIZATION

A. Motivation

With the seemingly paradoxical results of Slater and backflow wave functions yielding similar energies but requiring very different restrictions on the region of the iteration of the Green's function, the question of just how different the wave functions really are arises. Are these wave functions actually very similar or are they different in some fundamental but yet unseen way? To answer this question, we want a method to distinguish wave functions quickly, without having to perform a complete and expensive (hundreds of CPU hours on a supercomputer) energy calculation. In particular, we would like to understand how two wave functions can appear to have similar nodal surfaces, at least in some average sense, while having effects that would imply very different nodal surfaces. Since the one-body density matrix $n(r)$, as indicated above, is itself a measure of the change in the wave function for a given particle displacement r, this seems to be a reasonable place to start in comparing properties of wave functions.

The one-body density matrices $n(r)$ computed for both Slater and backflow variational wave functions after more than 500 000 passes, as shown in Fig. 1, are incredibly simi-

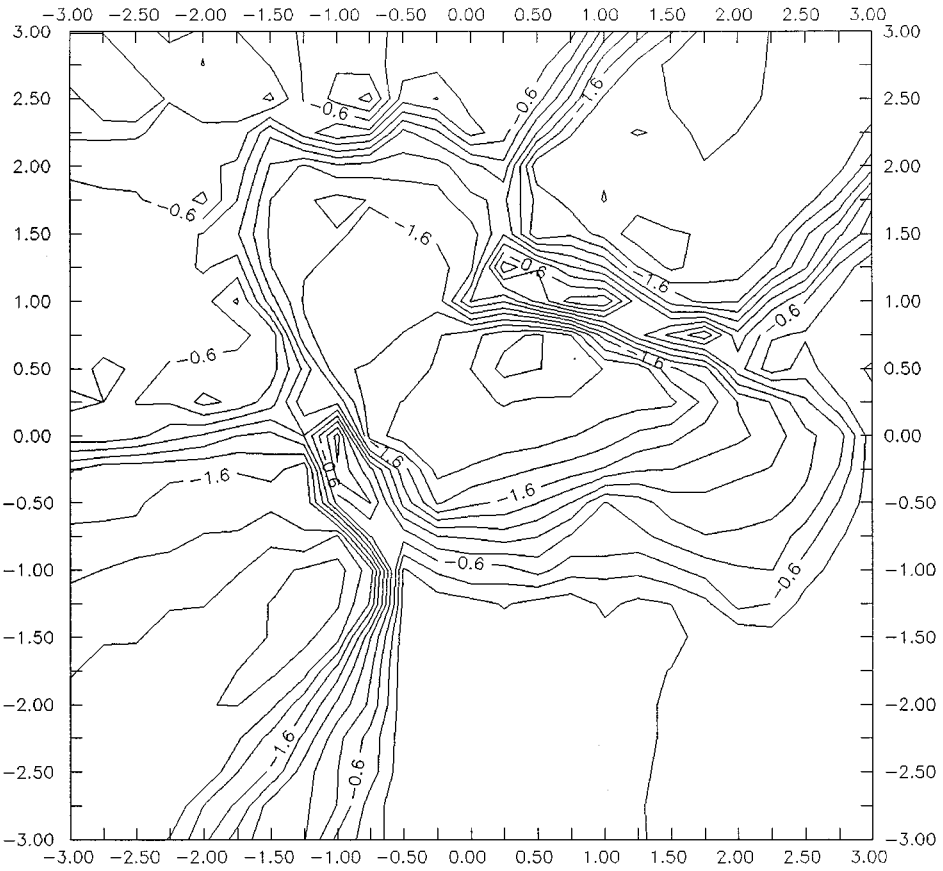

FIG. 5. Topological plot showing the lower half of the nodal volume generated from a backflow wave function.

lar. The region of $n(r)$ near the first zero crossing is enlarged in Fig. 2. As with the various energy results, there is very little evidence that the two wave functions differ from each other significantly. These curves suggest that the two wave functions might have very similar nodal surfaces since their zero crossings—in some sense a measure of the average distance to the nodal surface—are nearly the same. If this were to be the only information, one would be led to conclude again that the small but significant energy changes in Table I are due to subtle, perhaps imperceivable, changes in the nodal surface of the two wave functions. The $n(r)$ for each wave function was calculated by averaging over a few hundred random directions for every particle in a configuration and averaging over many such independent and well-separated configurations. Since we used the second method described above—moving a given particle in increments dr along a prescribed direction—we found that we could simultaneously capture information about two other quantities. We first computed the average distance a particle could be displaced without changing the sign of the overall wave function, averaging over all particles, all directions, and all configurations. We also computed the average of the smallest distance a particle could be displaced before changing the overall sign of the wave function, averaging over all particles and configurations only.

The results of these calculations are again paradoxical. The average distances a particle could move in any direction in a domain of constant sign are almost statistically indistinguishable for Slater and backflow wave functions

$$\langle r\rangle_{\text{Slater}} = 2.2 \pm 0.1\ \sigma,$$

$$\langle r\rangle_{\text{backflow}} = 2.1 \pm 0.1\ \sigma.$$

The distances here are in units of $\sigma = 2.566$ Å. This is completely consistent with the results displayed in Fig. 2, which shows a very slight reduction in the value of r for the first zero crossing for the backflow curve compared to the Slater curve.

On the other hand, the average of the minimum distance a particle could be displaced and still result in a sign change in a given configuration for backflow and Slater wave functions differs by more than two standard errors:

$$\langle r_{\text{min}}\rangle_{\text{Slater}} = 0.90 \pm 0.05\ \sigma,$$

$$\langle r_{\text{min}}\rangle_{\text{backflow}} = 1.15 \pm 0.05\ \sigma.$$

This result is consistent with the empirical result that constructing a spherical domain of constant sign in a fixed-node GFMC algorithm requires a much smaller radius for backflow wave functions than for Slater wave functions. Our numerical ''picture'' remained cloudy, despite hundreds of thousands of samples of r and the averaging of $n(r)$. We turned to visualization techniques as a means of extracting useful and insightful information from all of the calculations we have performed rather than simply averaging like quantities.

B. Method

Improving the efficiency of the fixed-mode implementation of the GFMC algorithm requires a deeper appreciation

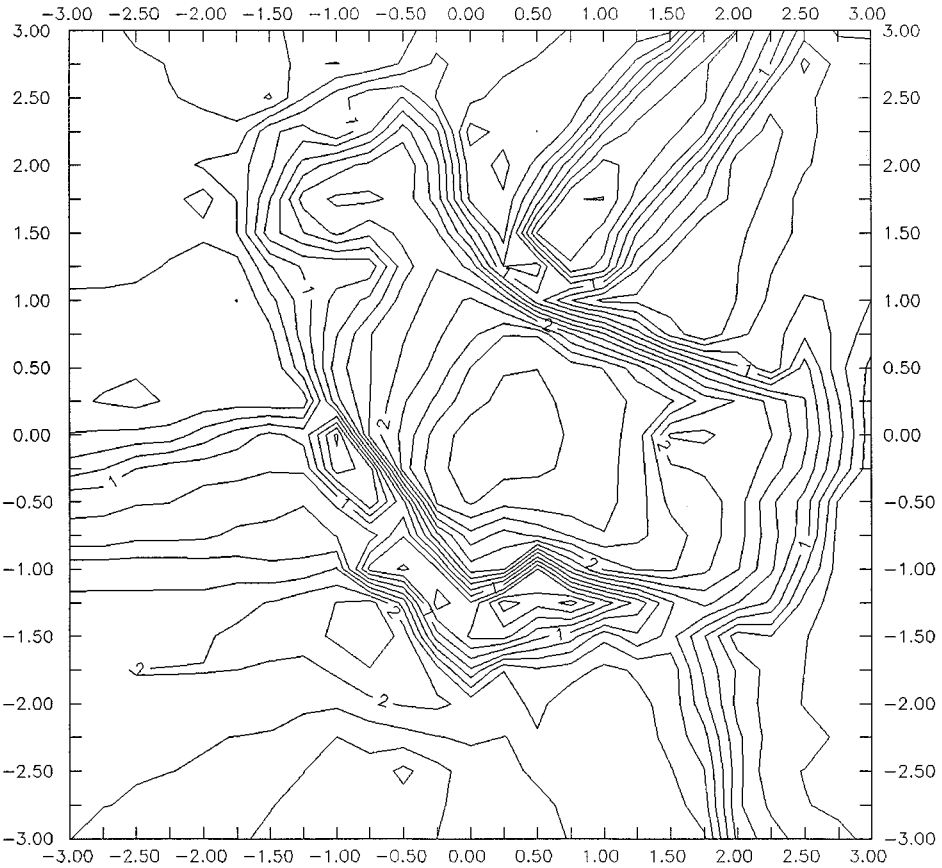

FIG. 6. Topological plot showing the upper half of the nodal volume generated from a backflow wave function.

of the subtleties of the many-body nodal surface. The algorithm itself, however, is built on expanding the Green's function for a single particle in a domain of constant sign around that particle. Examining the structure of the volume in which a single particle can be displaced without changing the overall sign of the wave function seems reasonable. The information to construct this volume can fall naturally out of the calculational scheme already described for computing $n(r)$.

For a given configuration, a random particle in the 54-particle system is chosen and the coordinate system is shifted so the chosen particle is placed at the origin, keeping intact the periodic boundary conditions imposed on the system. The surface of the volume in which that particle can move from the new origin without changing the overall sign of the wave function is then created by moving the chosen particle in small steps in prespecified directions. Successive steps are taken in a specific direction, the wave function being recalculated at each step and tested to see if it has flipped its sign and become negative. Once this sign change has occurred, the point is recorded and the particle ceases to march further in that direction. The particle then is returned to its origin and begins its march in the next designated direction. After the particle has been marched in all of the prespecified direc-

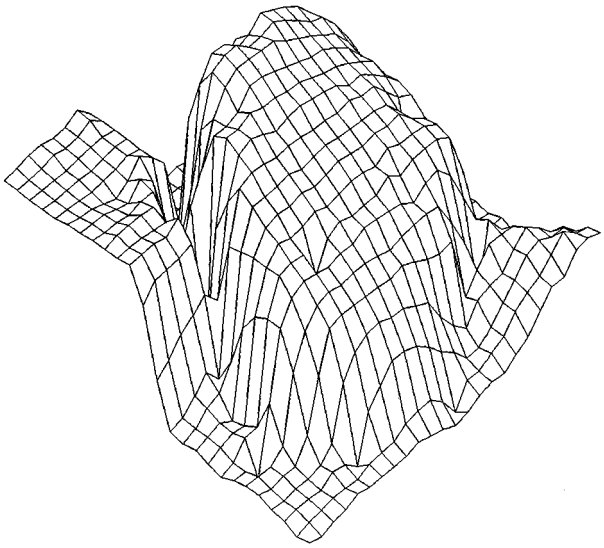

FIG. 7. SURFER surface plot of the same volume as in Fig. 4.

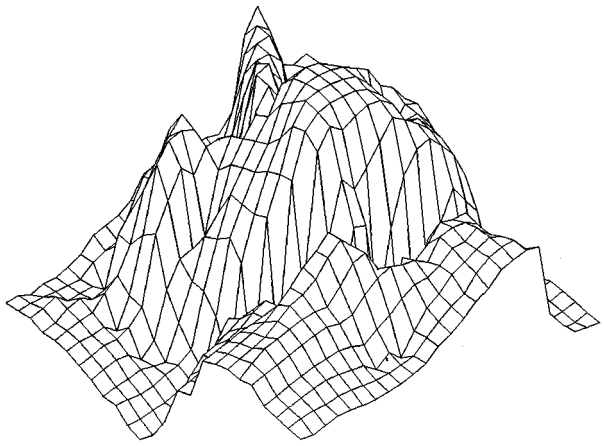

FIG. 8. SURFER surface plot of the same volume as in Fig. 6.

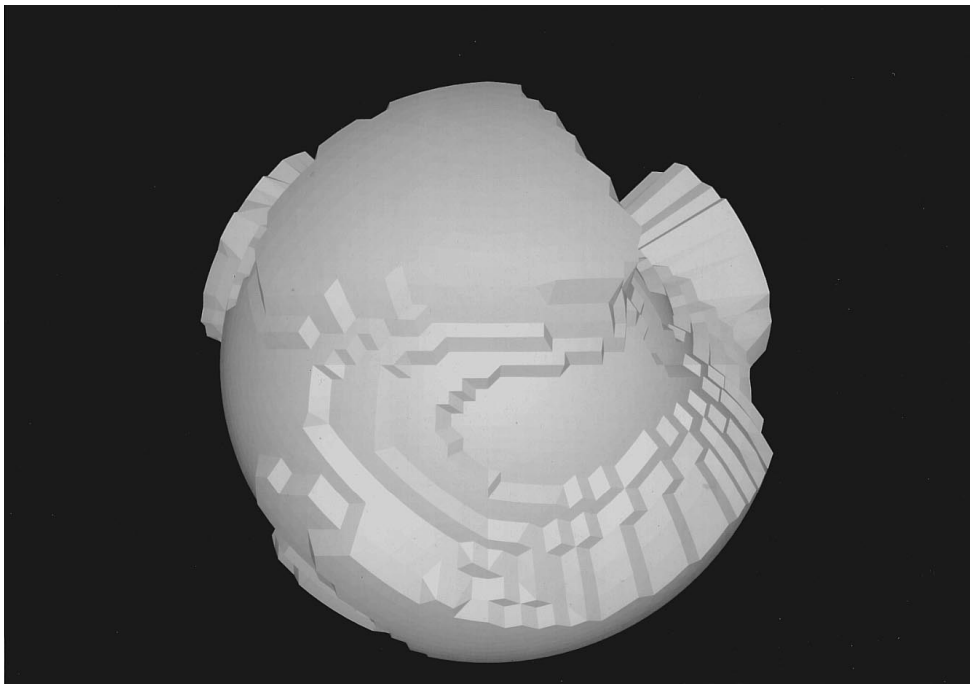

FIG. 9. WAVEFRONT rendering of the surface of a nodal volume generated from a Slater wave function.

tions, it is then intentionally marched in the direction of all other particles. All of the recorded points at which the wave function switched sign ultimately make up the surface of the local region of constant sign of the wave function for a single particle. Our method then is to construct such surfaces and to compare the various surfaces so constructed for configurations corresponding to similar and dissimilar wave functions. Different methods of generating the direction vectors were tried, including both randomly and uniformly distributed directions. In each case, we also searched specifically in the directions from the chosen central particle to every other particle in the configuration. While the surface of these domains of constant sign of the wave function is not the same as the many-body nodal surface, the surface is intimately related to nodal surface because the nodal surface completely determines its characteristics. At this point, the problem shifts to one of finding an appropriate way of visualizing such surfaces for purposes of comparison. We will refer to these surfaces as ''nodal volumes.''

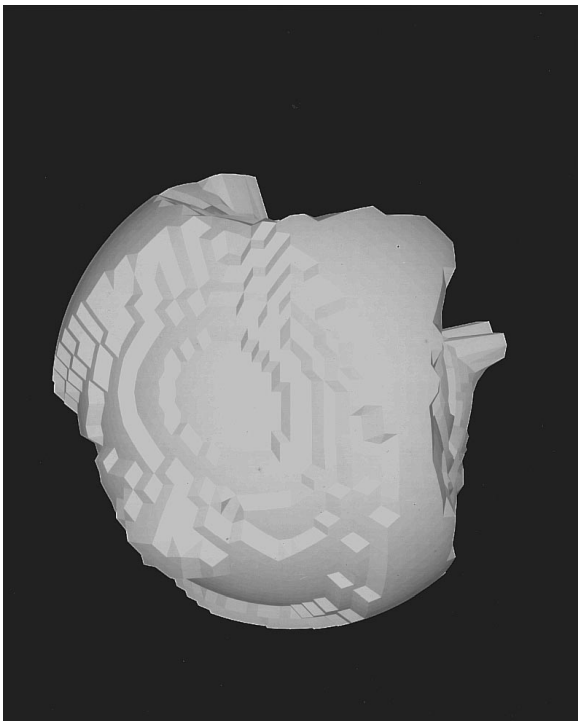

FIG. 10. WAVEFRONT rendering of the surface of a nodal volume generated from a Slater wave function. Same volume viewed from the same perspective as in Fig. 4.

IV. RESULTS AND DISCUSSION

We were able to evaluate several different graphics packages and platforms on which the software ran, yielding information about the relative merits of different visualizing methods. Our approach was to start with the simplest graphics package available to us and then to go to more advanced packages, applying what we learned along the way. We began with SURFER, a graphics package with multiple graphical modes running on a personal computer. Typical contour plots of the nodal volumes generated by TOPO, the topographical plot mode of SURFER, are shown in Figs. 3–6. The differences between the two surfaces would appear as differences in the deformations of the contours from those of a perfectly spherical surface. Plots for different particles of configurations for the Slater wave functions showed marked similarities. As seen in Figs. 3 and 4, Slater wave functions are characterized by relatively smooth contours on the surface, that is, contours that are rather evenly spaced and somewhat symmetrical. In most cases the Slater surfaces have an overall continuous appearance. In contrast, as typified by Figs. 5 and 6, the surfaces generated from the backflow wave function have rather constricted and rough contours, suggesting a more rapidly changing wave function. Backflow-related surfaces from different points and configurations were also more sharply varying, one from another, in comparison to Slater plots.

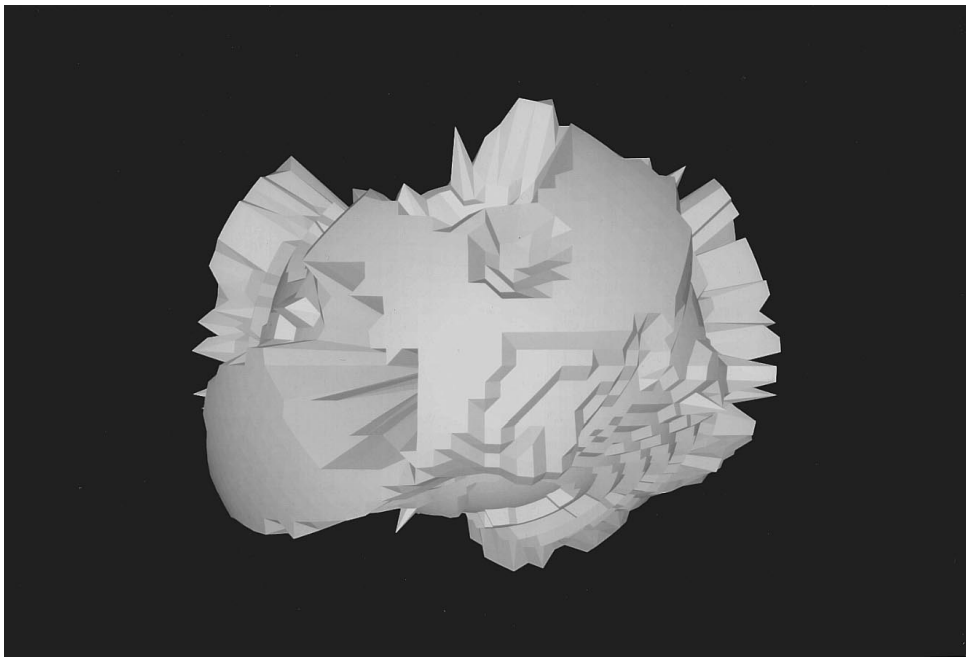

FIG. 11. WAVEFRONT rendering of the surface of a nodal volume generated from a backflow wave function.

Since certain features of the topological plots depend strongly on the random orientation of the nodal volume, an alternative visualization scheme was desired that permits looking at a three-dimensional rendering of the whole volume. Accordingly, we then studied images created by SURF mode of SURFER, which generates an isosurface through a set of nonredundant points (which we had). Although we were still restricted to looking at one hemisphere at a time, the interpolated surfaces served quite well to train us to interpret the topological plots. Representative plots for a surface of a Slater nodal volume and a backflow nodal volume are given in Figs. 7 and 8, respectively. These plots, along with the topological counterparts, led us to describe the backflow volumes to be decidedly more constricted than Slater volumes. The SURF plots also suggested that some of the sharp features in the TOPO plots of the backflow nodal volumes were possibly sharp peaks to go along with the sharp crevices. Because SURF was producing an isosurface smoothed over a rectangular grid, we could not be sure that some of these features were not artifacts from SURF.

We then considered a full three-dimensional rendering of the surfaces using two graphics packages named GALAXY and WAVEFRONT. These packages offered the possibility of real time rotation of the full volume, which allowed for easier comparison and differentiation of various surfaces. Our results from WAVEFRONT are also shown in Figs. 9–12. The images in Figs. 9 and 10 correspond to Slater nodal volumes, and those in Figs. 11 and 12 correspond to backflow nodal volumes. Figures 10 and 12, for comparison, correspond to exactly the same perspectives as the topology plots in Figs. 4 and 6. The most notable feature, present in the backflow images and nearly absent in the Slater views, are sharp spikes and deep localized sink holes, as in Figs. 11 and 12. With these views, taken together, one can immediately ''see'' how two surfaces could have nearly the same average radius while having sharply different minimum cross sections. Physically, the constricted volume surrounding a single particle is related to the greater localization of the atom in the liquid with the backflow correlations than without them. The sharply constricted volumes associated with the backflow wave function also explain the smaller domains that were needed to implement the fixed-node GFMC algorithm. Furthermore, in the computation of $\langle r_{\min} \rangle$ it was nearly always the case that the direction of $\langle r_{\min} \rangle$ for the Slater nodal volume was consistent with the direction of another particle. For the backflow volumes, more than a third of the time the direction of $\langle r_{\min} \rangle$ was essentially random, suggesting a subtle, correlated, many-body effect.

FIG. 12. WAVEFRONT rendering of the surface of a nodal volume generated from a backflow wave function. Same volume viewed from the same perspective as in Fig. 6.

Having viewed many such computer generated volumes and noting the similarities for such volumes generated from the same wave function, we are confident in our characterizations, at least with regard to comparing Slater-type wave functions with wave functions incorporating backflow in the determinant.

V. IMPACT ON FUTURE DIRECTIONS IN THE QUANTUM MONTE CARLO METHOD

A key result of this work is the striking visual evidence that the local contributions to the many-body nodal surface, as measured by the volumes studied here, are *very* different for Slater and backflow-type wave functions. We would conclude that it has taken a large change in the nodal structure to produce rather small changes in the energy and almost undetectable changes in the other ground-state properties. As a result, rather than looking for small changes in the parameters in the wave function to achieve any further improvement, we need to explore new families of parametrizations.

The quantum Monte Carlo method has achieved the reputation of being accurate, and with appropriate refinements, key implementations of its fundamental algorithms can also be efficient. Consequently, variational and Green's function Monte Carlo methods are no longer relegated to the service role of benchmarks for approximate calculational methods, but they can provide otherwise inaccessible insight to the microscopic structure of matter.

With the nodal volume visualization that have come out of the present work, we have identified a principle bottleneck in improving one important implementation of the GFMC method, namely, the fixed-node approximation. While backflow correlations yield a lower variance calculation, they do so at the considerable expense of restricting the size of the domains in which the Green's function may be expanded. This had gone previously unexplained, because the only available information prior to this work incorporated averages over many volumes instead of examining the morphology of a single volume, and these averages have been misleading. Current implementations to the fixed-node GFMC method estimate the distance to the nearest part of the nodal surface only in the directions of other particles. Our work shows that this method might be improved by considering directions away from particles as well.

For the many-fermion problem, a trade-off can now be tested as to the overall efficiency of slow, but low variance quantum simulations versus fast but high variance simulations. A goal we have is to correlate morphology with energies: we seek a wave function with a nodal structure resulting in a low variance calculation, a lower energy, and a less constrained domain of constant sign.

We end by returning to a point of emphasis from our introduction: the visualizations we have explored are important because they have helped us understand an important piece of the *process* to improve an algorithm and not just in presenting a *result*. Efficient use and integration of a variety of high performance computing platforms enabled this work to be done sooner than it otherwise could have been done conventionally, with more insight than we ourselves imagined, resulting in a better understanding of the physics of strongly correlated quantum systems and the algorithms that are used to study them.

ACKNOWLEDGMENTS

Computation resources on IBM 3090 and RISC System/6000 were provided by IBM Corporation, High Performance Computing Solutions Development, Kingston, New York. We would like to thank Rich Anderson and the staff at IBM-Kingston, without whose support and encouragement this work would not have been possible. We would also like to thank Clifford Pickover and Michael Henderson of IBM and Tom Palmer of CRI for their generous help in producing the final images that are included in this work. We also thank Brent Han for his contribution to this work.

[1] R. M. Panoff and J. Carlson, Phys. Rev. Lett. **62**, 1130 (1989).
[2] R. M. Panoff, in *Condensed Matter Theories, Vol. II*, edited by P. Vashista, R. Kalia, and R. Bishop (Plenum, New York, 1987).
[3] P. A. Whitlock and R. M. Panoff, Can. J. Phys. **65**, 1409 (1987).
[4] M. A. Lee, K. E. Schmidt, M. H. Kalos, and G. V. Chester, Phys. Rev. Lett. **46**, 728 (1981).
[5] K. E. Schmidt, M. A. Lee, M. H. Kalos, and G. V. Chester, Phys. Rev. Lett. **47**, 807 (1981).
[6] E. Manousakis, V. R. Pandharipande, and Q. N. Usmani, Phys. Rev. B **31**, 7022 (1985).
[7] J. P. Bouchard and C. Lhuillier, Europhys. Lett. **3**, 1273 (1987).
[8] R. M. Panoff, in *Recent Progress in Many Body Physics*, edited by Y. Auishai (Plenum, New York, 1990).
[9] J. Zabolitzky, in *Progress in Particle and Nuclear Physics*, edited by A. Faessler (Pergamon, Oxford, 1986), Vol. 16; Proceedings of the Conference on Frontiers of Quantum Monte Carlo [J. Stat. Phys. **43**, 211 (1986)].
[10] D. M. Ceperley and B. J. Alder, Phys. Rev. Lett. **45**, 566 (1980).
[11] J. W. Moskowitz, K. E. Schmidt, M. A. Lee, and M. H. Kalos, J. Chem. Phys. **77**, 349 (1982).
[12] R. A. Aziz, V. P. S. Nain, J. S. Cerley, W. L. Taylor, and G. T. McConville, J. Chem. Phys. **70**, 4330 (1979).
[13] M. H. Kalos, M. A. Lee, P. A. Whitlock, and G. V. Chester, Phys. Rev. B **24**, 115 (1981).
[14] Eugene Feenberg, *Theory of Quantum Fluids* (Academic, New York, 1969).
[15] E. Krotscheck, R. A. Smith, J. W. Clark, and R. M. Panoff, Phys. Rev. B **24**, 6383 (1981).

[16] V. R. Pandharipande and H. A. Bethe, Phys. Rev. C **7**, 1312 (1972).
[17] R. M. Panoff and P. A. Whitlock, in *Momentum Distributions*, edited by R. Silver (Plenum, New York, 1989).
[18] N. Metropolis, A. W. Rosenbluth, M. N. Rosenbluth, A. M. Teller, and E. Teller, J. Chem. Phys. **21**, 1087 (1953).
[19] M. H. Kalos, D. Levesque, and L. Verlet, Phys. Rev. A **9**, 2178 (1974).
[20] D. M. Ceperley and M. H. Kalos, in *Monte Carlo Methods in Statistical Physics*, edited by K. Binder, Topics in Current Physics Vol. 7 (Springer, Berlin, 1979), Chap. 4.
[21] J. Carlson and M. H. Kalos, Phys. Rev. C **32**, 1735 (1985).